

Microstructure characterization of kerogen in mature shale: Molecular investigation of micropore development

Chu Zhang^{a,b}, Yanbin Yao^{a,b,*}, Derek Elsworth^c, Dexun Liu^d, Yiwen Ju^e, Yuguang Dong^{a,b}, Shun Ye^{a,b}

^a School of Energy Resource, China University of Geosciences, Beijing, 100083, China

^b Beijing Key Laboratory of Unconventional Natural Gas Geological Evaluation and Development Engineering, China University of Geosciences, Beijing, 100083, China

^c Department of Energy and Mineral Engineering, Pennsylvania State University, University Park, PA, 16802, USA

^d Research Institute of Petroleum Exploration and Development, Beijing, 100083, China

^e Key Laboratory of Computational Geodynamics, College of Earth and Planetary Sciences, University of Chinese Academy of Sciences, Beijing, 100049, China

ARTICLE INFO

Keywords:

Kerogen
Molecular simulation
Gas shale
Micropores in shale
Macromolecular structure

ABSTRACT

Micropores (<2 nm) are commonly well developed in shale kerogen, which plays an important role for generation and transport of gas in shales. However, the mechanism of micropores development in kerogen structure has not been fully investigated. In this study, we provide an improved methodology to construct 3-D models of kerogen structure, then we construct such molecular models of kerogen for two well-known shales (the Marcellus shale from USA and Shanxi Formation shale from China), and finally we discussed the influences of chemical composition and disorder degree on the formation of micropores in the mature kerogens. Results show that loss of aliphatic structures and the increase in aromatic structures are favorable for the development of micropores. By comparing the kerogen models of M-1 and SX-2, we found that the morphology of micropores in aliphatic structures is more complex than that in aromatic structures. Analyses from ¹³C Nuclear Magnetic Resonance (NMR) and Raman spectroscopy indicate that apart from chemical compositions, spatial arrangement of structural groups can also affect the development of micropores. For mature kerogen with a large proportion of aromatic rings, disordered aromatic rings are favorable for the development of micropores.

1. Introduction

Shale gas is generally regarded as self-sourced and, while some gas is stored in the free space of macropores (>50 nm), most is adsorbed in organic nanopores or on the surface and interlayer pores of clay (Loucks et al., 2009). Most hydrocarbon gas is generated during thermal maturation with organic-matter hosted pores providing storage space for free gas and also specific surface area for adsorbed gas (Liu et al., 2018; Yao et al., 2019). Even though the total organic carbon (TOC) content in shales is usually less than 10% in shale, it has been shown that almost half of the gas is adsorbed by the organic matter (OM) (Rexer et al., 2014). The OM of the shale is mainly composed of kerogen and bitumen (Tissot et al., 1974). Thus, the study of kerogen structure is significant for our understanding of the development of OM porosity and its relationship with the generation and storage of shale gas.

Many advanced experimental methods have been applied to study the chemical structures of kerogen over several decades. For example,

Tissot et al. (1974) simulated the natural degradation of kerogen during burial process, by using the thermogravimetric analysis and infrared spectrometry. Based on Fourier transform infrared (FT-IR), Borrego et al. (2000) characterized the proportion of functional groups of shale kerogen during pyrolysis, and they found that the proportion of oxygen-bearing functional groups are abundant in immature samples. Using solid-state ¹³C NMR, X-ray photoelectron spectroscopy (XPS), FT-IR, and X-ray diffraction (XRD), Tong et al. (2011) evaluated the structural characteristics of carbon skeleton and heteroatoms in oil shale kerogen, and they found that oxygen in C–O and C–OH groups tend to bound with aromatic carbons. Ungerer et al. (2015) constructed several molecular structure models of kerogen based on XPS and ¹³C NMR, and quantitatively predicted thermodynamic properties (e.g., heat capacity) of models through molecular dynamic simulation. By combining XRD, FT-IR and high-resolution transmission electron microscopy (HRTEM), Wang et al. (2019) found that the average lateral sizes (L_a) and stacking heights (L_c) of the kerogen macromolecular structure in Longmaxi shale

* Corresponding author. School of Energy Resource, China University of Geosciences, Beijing, 100083, China.

E-mail address: ywb@cugb.edu.cn (Y. Yao).

<https://doi.org/10.1016/j.jngse.2021.104239>

Received 30 May 2021; Received in revised form 28 August 2021; Accepted 6 September 2021

Available online 9 September 2021

1875-5100/© 2021 Elsevier B.V. All rights reserved.

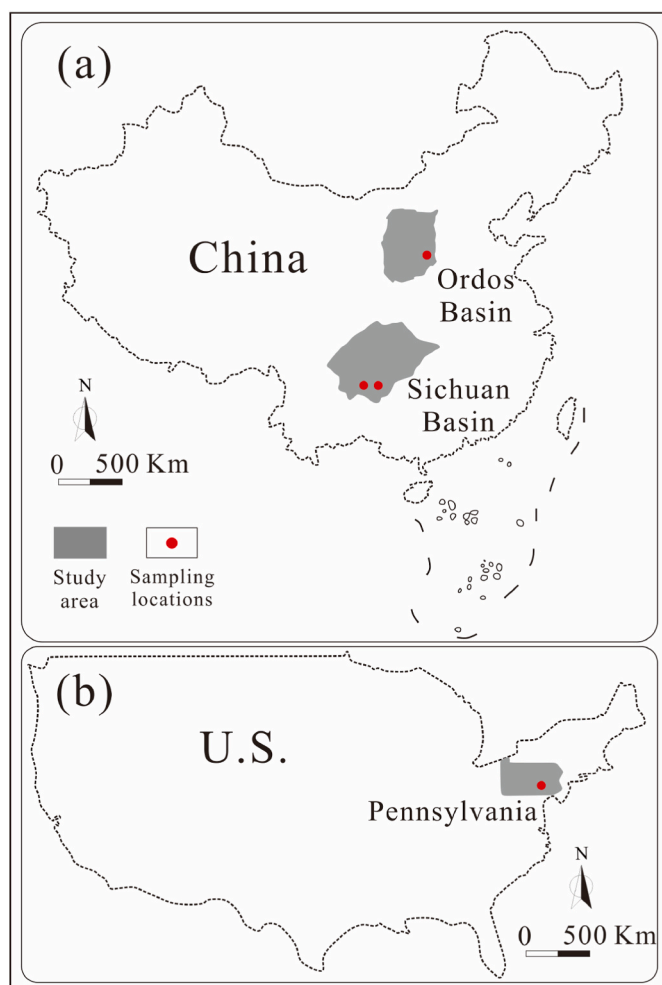


Fig. 1. Sampling locations for Longmaxi, Shanxi (a) and Marcellus shales (b).

Table 1
Sampling locations.

Sample ID	Formation	Sedimental environment	Location	Sample source
SX-1	Permian	Transitional	Well 3-4 in Daning-Jixian block	Drill core
SX-2	Shanxi formation			Drill core
LMX-2	Silurian Longmaxi formation	Marine	Lujiao profile in Pengshui area	Outcrop
LMX-3			Shuanghe profile in Changning area	Outcrop
M-1	Devonian Marcellus shale		South central Pennsylvania	Outcrop

gradually increased during maturation, which is favorable for the formation of micropores.

Recently, many 3-D models of kerogen structures were widely used in the study of microstructure characteristics and fluid dynamics of kerogen. For example, using graphite slit model and grand canonical Monte Carlo (MC) simulations, Mosher et al. (2013) found that the excess adsorption amount decreases with increasing pore size. In contrast, Zhang et al. (2019) used similar model but they found that the excess adsorption amount increases with increasing pore size at < 2 nm, while the excess adsorption amount decreases with increasing pore size at > 2 nm. For these simulation studies, it is extremely important to construct a realistic 3-D model of kerogen structure. There are various molecular models of kerogen that have been constructed by different

researchers. For example, Lille et al. (2003) constructed a molecular model of Estonian kukersite kerogen by ^{13}C NMR spectrum. Similarly, Using ^{13}C NMR, X-ray and XPS, Ungerer et al. (2015) built model units of kerogens with different OM types. Moreover, Bousige et al. (2016) constructed more realistic molecular models of mature and immature kerogens, while Xiong et al. (2017) adopted graphite with functional groups to simplify kerogen model.

Although previous researchers have completed a broad array of studies on the simulation of the molecular structure of kerogen, there are at least two clear deficiencies in these studies. First, most existing simulation studies adopted the models of kerogen structure proposed by Ungerer et al. (2015) (Huang et al., 2019; Zhao et al., 2018), with some researchers simply adopting graphite as an alternate to bulk kerogen in order to idealize OM porosity (Mosher et al., 2013; Xiong et al., 2017). However, graphite does not exactly match the chemical and physical properties and structural characteristics of bulk kerogen, and Ungerer's model is not representative of all kerogen types. Thus, it is necessary to construct more realistic models of kerogen structure for different shale types. Second, there are many methods for constructing models of kerogen structures, however, most of these methods have difficulty in replicating the real kerogen properties. For example, some methods only consider the pore morphology but not kerogen molecular structure (Ju et al., 2019), while others focus on the comparison of simulated density and experimental data but neglect the influence of kerogen type and thermal maturity (Huang et al., 2018).

In this study, five shale samples were collected from Shanxi, Longmaxi and Marcellus Formations. We performed Raman spectroscopy, ^{13}C NMR and CO_2 adsorption experiments to investigate the microstructure of kerogen. First, we provided an improved methodology for constructing a 3-D model of kerogen structure. Based on this methodology, taking the Shanxi and Marcellus Formation shales as examples, we then created two 3-D models of kerogen structure. Finally, we discussed the influence of chemical structure on the development of micropores in mature kerogens.

2. Samples and analytical methods

2.1. Samples

To investigate the microstructural differences among different shale kerogens, five shale samples were collected from three well-known basins: the Middle Devonian Marcellus Formation in the Appalachian Basin in the USA, the Permian Shanxi Formation shale in the southeastern Ordos Basin in China, and the Silurian Longmaxi Formation shale in the Sichuan Basin in China (Fig. 1). Both the Longmaxi and Marcellus are major targets for shale gas production, while the Shanxi Formation has shown good prospects for shale gas exploration. Samples SX-1 and SX-2 were obtained at a depth of ~ 2150 m in an exploration well in the Daning-Jixian block in the southeastern Ordos Basin, while the remaining samples were collected from outcrop (Table 1). Both the Longmaxi and Marcellus shales were collected from outcrop, because it is difficult for us to collect core sample in the related gas fields.

2.2. Analytic methods

The total organic carbon (TOC) content was measured according to the China National Standard GB/T19145-2003. The instrument used was a CS-230 carbon/sulfur analyzer produced by LECO Company, USA. The sample was crushed to #80–100 mesh. The powdered shale was treated with HCl to first dissolve the carbonates, and then pyrolyzed to 813.15 K.

The average vitrinite reflectance (R_o) was determined according to SY/T5124-2012 to measure vitrinite reflectance in whole rock. An Axio Imager Mlm instrument was used, with magnification of objective lens at $50 \times 0.85_{\text{Oil}}$ (oil immersion). The average vitrinite reflectance was calculated based on 15–30 random measurements. Due to the absence of

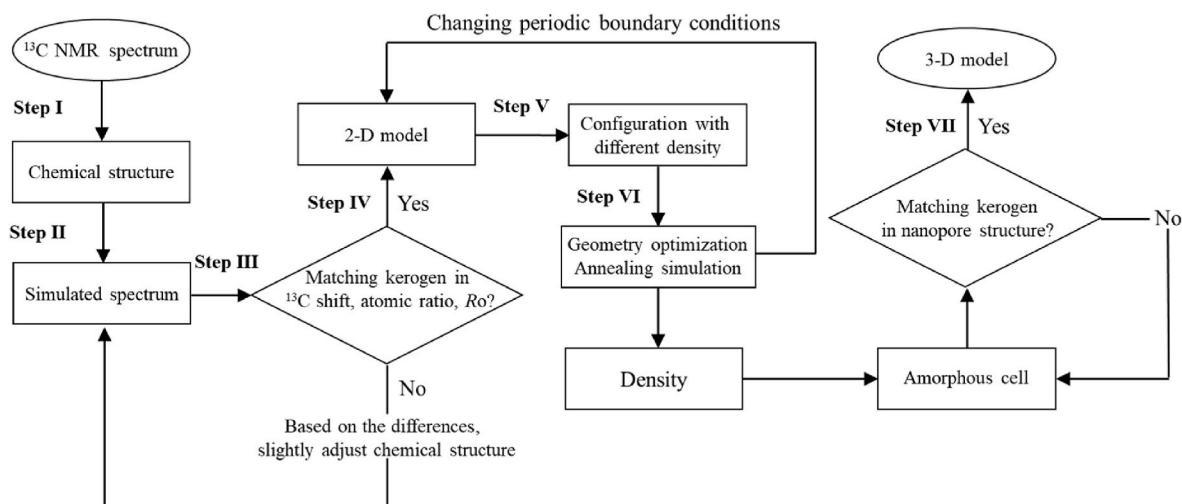


Fig. 2. Workflow for constructing 3-D model of kerogen structure.

Table 2
Geochemical properties of the collected shale samples.

Sample ID	OM types	TOC (wt.%)	Ro (%)	EqVRo (%)
SX-1	III	1.42	1.67	–
SX-2	III	7.56	2.02	–
LMX-2	I	0.8	1.27	1.18
LMX-3	I	3.51	1.38	1.25
M-1	II	6.85	1.13	–

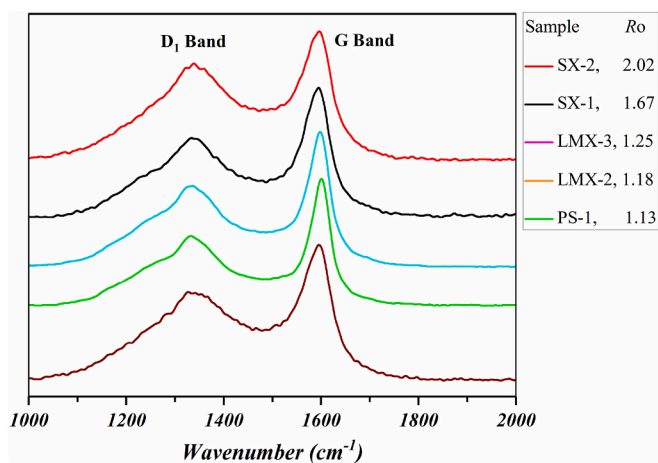


Fig. 3. Raman spectra of kerogen samples.

Table 3
Band parameters of the Raman spectra.

Sample ID	ν^{D1} (cm^{-1})	ν^G (cm^{-1})	RBS (cm^{-1})	I_{D1}	I_G	I_{D1}/I_G
SX-1	1333	1595	262	530	870	0.61
SX-2	1339	1596	257	564	749	0.75
LMX-2	1332	1600	268	4699	8535	0.55
LMX-3	1335	1599	264	2961	4944	0.60
M-1	1327	1595	268	539	828	0.65

ν is the central positions of the G and D_1 bands; RBS is the differences between the central positions of G and D_1 bands; I is the intensities of the G and D_1 bands.

vitrinite in Silurian Longmaxi Formation shale, the solid bitumen reflectance is considered for reflectance measurement (Landis and Castaño, 1995). The conversion formula of equivalent vitrinite

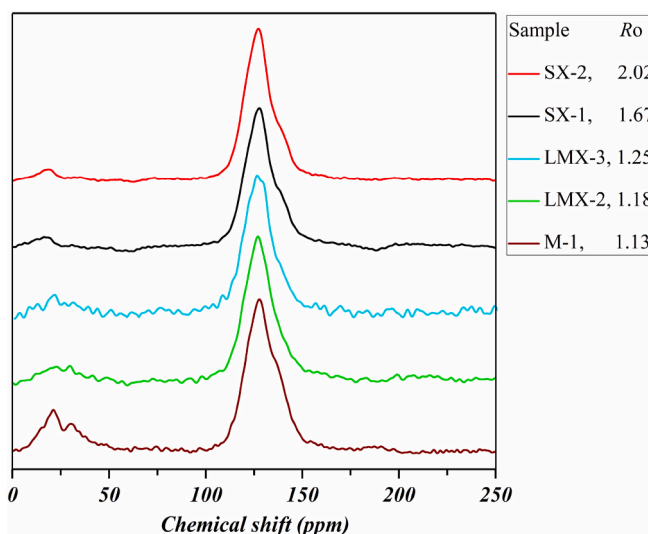


Fig. 4. ^{13}C NMR spectra of kerogen samples.

reflectance ($EqVRo$) and bitumen reflectance (BRO) is (Jacob, 1989):

$$EqVRo = 0.618BRO + 0.4 \quad (1)$$

A standard kerogen isolation pretreatment was performed according to the Chinese National Standard GB/T19144-2010. The carbonate and silicate minerals were removed by adding 20% HCl, and a mixture of 20% HCl and 40% HF, respectively. Moreover, 20% HCl and zinc particles were used to remove the pyrite, and then the solid bitumen was removed by chloroform extraction. After the pretreatments, the isolated kerogen was analyzed by means of Raman and ^{13}C NMR spectroscopy and gas adsorption. Among them, the Raman and ^{13}C NMR spectroscopy were utilized to characterize the chemical structure of kerogens, while gas adsorption experiment was used to characterize micropores structure.

Raman spectroscopy was carried out on a Senterra instrument manufactured by the Bruker Company, Germany. Kerogen samples were pulverized to about #200 mesh. The scan wavenumber range was 1000–2000 cm^{-1} and the experimental resolution was 9–18 cm^{-1} . The laser wavelength was 532 nm and the laser power was 5 mW. The integration time was 2 s (Liu et al., 2013).

^{13}C NMR spectroscopy was used to characterize the carbon skeleton of kerogens. The instrument used was an INOVA300 spectrometer

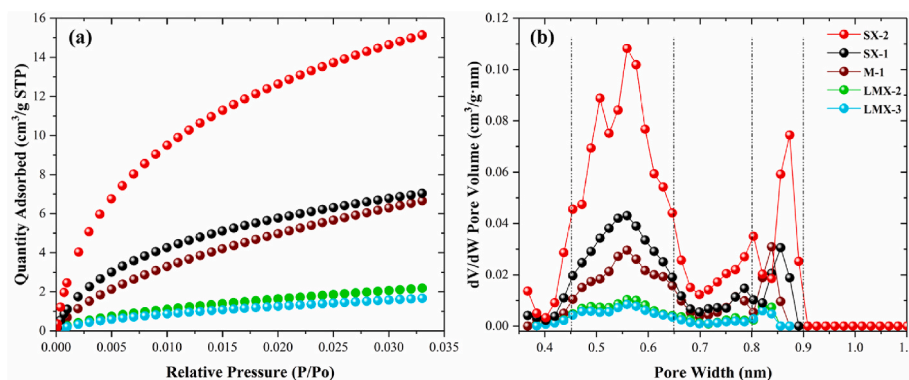


Fig. 5. CO₂ adsorption isotherms (a), and micropore size distribution (b).

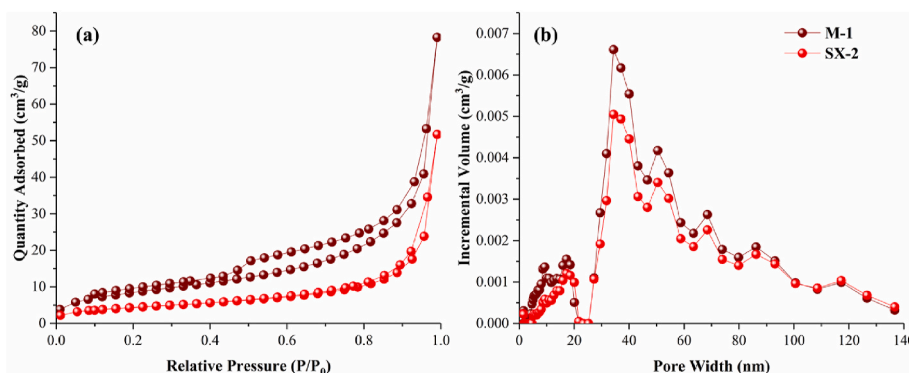


Fig. 6. N₂ adsorption/desorption curves (a), and pore size distribution (b).

Table 4

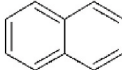
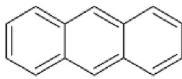
¹³C NMR parameters of different kerogen samples.

Sample ID	f_{al}^*	f_{al}^H	f_{al}^O	f_a^H	f_a^B	f_a^S	f_a^P	f_a^c	X_{BP}	X_b
	0–22	22–50	50–90	90–129	129–137	137–150	150–165	>165		
SX-1	4.17	2.80	3.56	48.94	16.75	7.85	3.44	12.48	0.28	0.19
SX-2	4.24	2.69	3.01	53.37	20.24	5.38	2.87	8.20	0.33	0.23
LMX-2	2.35	9.88	2.81	49.14	10.58	9.70	3.89	11.64	0.17	0.13
LMX-3	5.95	6.38	2.97	53.13	8.70	8.45	3.23	11.17	0.14	0.11
M-1	10.57	8.34	2.67	48.46	11.46	10.13	2.15	6.22	0.19	0.15

f_{al}^* : total sp³ hybridized carbon; f_{al}^* : CH₃ or quaternary carbon; f_{al}^H : aliphatic CH or CH₂; f_{al}^O : aliphatic carbon bonded to oxygen; f_a^* : aromatic carbon; f_a^H : protonated aromatic carbon; f_a^B : aromatic bridgehead carbon; f_a^S : alkylated aromatic carbon; f_a^P : aromatic carbon bonded to hydroxyl or ether oxygen; f_a^c : carbonyl groups or carboxyl groups; X_{BP} : ratio of aromatic bridge carbon to aromatic peripheral carbon; X_b : average size of aromatic ring.

Table 5

X_{BP} in different aromatic rings.

Aromatic ring sized	Aromatic bridge carbon	Aromatic peripheral carbon	X_{BP}
	0	5	0
 2 × 2 sized	2	8	0.25
 3 × 3 sized	4	10	0.4

produced by the Varian Company, USA. Observations were made with a sampling time of 0.05 s, cycle delay time of 4 s, and with 2000–4000 time scans (Hiroyuki and Ikuo, 2004). The total sidebands suppression technique was applied to obtain semiquantitative compositional information (MAS = 3 kHz, contact time = 1 ms, recycle delay = 1 s). Peak fitting method provided by Patience et al. (1992) was used to determine the chemical compositions of kerogen.

CO₂ and N₂ adsorption experiments were utilized to analyze the microporous structure using an ASAP 2460 Surface Area and Porosity Analyzer produced by Micromeritics, USA. Before the experiment, the powdered kerogen was degassed in a vacuum at a temperature <100 °C for 12 h to remove impurities. The analysis bath temperature of CO₂ and N₂ adsorption were 273.15 K and 77 K, respectively. For CO₂ adsorption experiment, Density Functional Theory (DFT) and Dubinin-Radushkevich models were used to determine pore size distribution and micropore volume, respectively (Nguyen and Do, 2001). For N₂ adsorption experiment, Brunauer-Emmett-Teller (BET) model were employed to calculate specific surface area (Gregg et al., 1967). Note

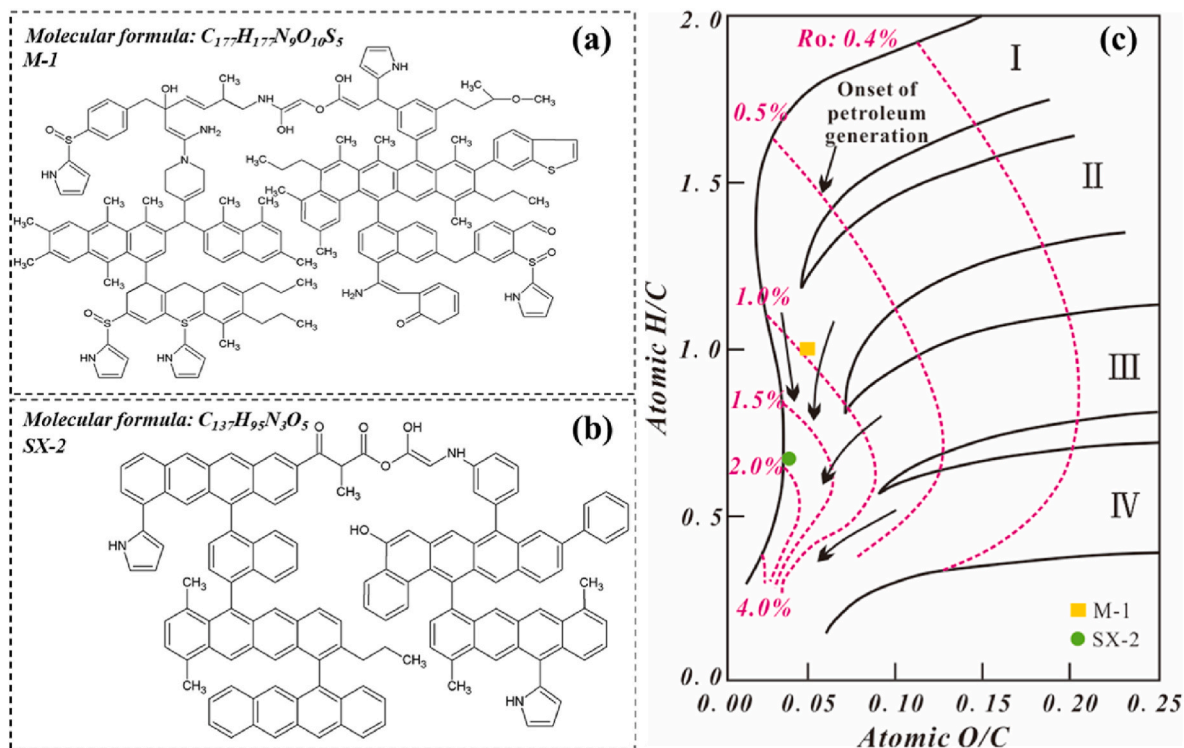


Fig. 7. 2-D models (a and b), and organic geochemical information (c: modified from Tissot et al. (1974)).

Table 6

Comparison of experimental and simulated data on the structural properties of models.

Structural parameters	M-1		SX-2	
	Model	Experimental ^a	Model	Experimental
Density (g/cm ³)	1.04	1.0–1.15	1.16	1.14 ± 0.02
H/C	1	1.19	0.69	0.56
O/C	0.057	0.08	0.036	0.04
<i>f_a</i> (%)	71.75	77.55	90.51	89.29
<i>f_{al}</i> [*] (%)	24.86	21.59	9.49	9.94
Micropore volume (cm ³ /g)	0.020	0.021	0.048	0.051
Specific surface area (m ² /g)	22.99	31.07	15.47	15.75

^a The experimental densities and atomic ratios are obtained from the reported data.

that since the specific surface area calculated from N₂ adsorption is used for the construction of kerogen models, the N₂ adsorption experiment is only carried out on M-1 and SX-2 samples.

3. Methodology for kerogen model construction

3.1. Construction based on experimental data

In this study, we provide an improved methodology to construct 3-D models of kerogen structure based on the experimental data including the chemical compositions (from ¹³C NMR), organic geochemistry data (atom ratio, Ro and OM types), density, and pore characteristics (from gas adsorption analysis). The detailed construction process is given as follows (Fig. 2):

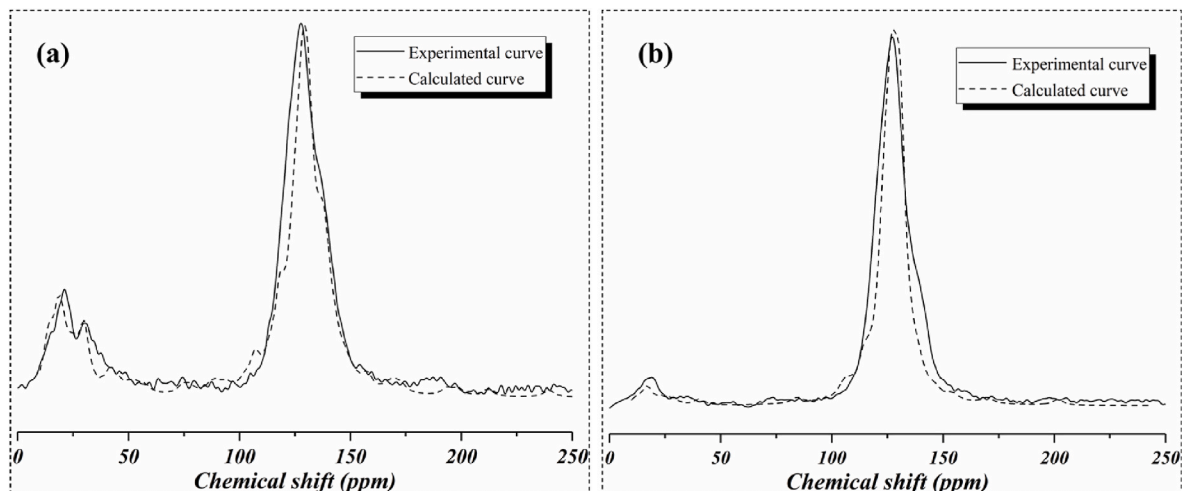


Fig. 8. Comparison of ¹³C NMR spectra between the calculated curve and the experimental curve (a: M-1; b: SX-2).

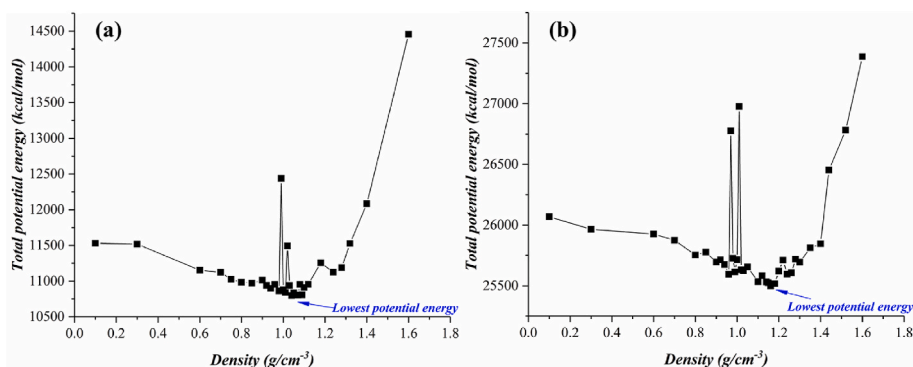


Fig. 9. Relationship of the total potential energy vs. density after annealing simulation (a: M-1; b: SX-2).

Table 7

Compare of the thermodynamic properties of the kerogens that are modeled based on Ungerer et al. (2015) models and this study.

Thermodynamic parameters	M-1		SX-2	
	Model of this study	Ungerer's model for Type II-A kerogen	Model of this study	Ungerer's model for Type III -A kerogen
Lowest potential energy (kJ/g)	1.6	/	5.7	/
Kinetic energy (kJ/g)	0.5	/	0.5	/
Total energy (kJ/g)	2.1	1.9	6.2	3.9
Heat capacity (J/g/K)	0.7	1.4	2	1.5
Total enthalpy (kJ/g)	2.4	/	6.5	/

- I) Deconvolution of the ^{13}C NMR spectrum is used to calculate the relative content of carbon structures (aliphatic carbons, aromatic carbons, etc.) in the kerogen.
- II) The initial version of the 2-D kerogen structure model is constructed using ACD Labs Pro software based on the carbon structures from ^{13}C NMR. Meanwhile the quantities of H and O atoms are determined by matching experimental data from the literature.
- III) The ^{13}C shift in the 2-D kerogen structure model is simulated in gNMR software, and the differences of ^{13}C shift between the simulated results and the experimental ^{13}C NMR curves are obtained.
- IV) The 2-D kerogen structure is modified by returning to the Step II until the ^{13}C shift from simulation agrees well with that from experiment.
- V) During the construction of the 3D model, a periodic box of cell generated by adding periodic boundary conditions to the 2D model is used to describe the amorphous structure of kerogen. A series of 3-D models of kerogen structure with different densities are generated in Materials Studio software by adding different periodic boundary conditions to the 2-D models of kerogen structure obtained in Step IV.
- VI) The configuration with the lowest local energy is obtained after optimization of the geometry. Annealing simulation is performed to calculate the density at the point of minimum potential energy.
- VII) Based on the density calculated in Step VI, a periodic boundary condition is again added to the model of 2-D kerogen structure. The final 3-D kerogen structure is generated by matching nanopore structure obtained from gas adsorption experiments.

3.2. Simulation details

The simulation was performed in Materials Studio (2017) (MS, 2017), from the Accelrys Company. The local energy minimum configuration of the 2-D kerogen structure model was obtained after optimization of geometry in the Forcite module. The algorithm used was the Smart method. The force field is Compass II, and the cutoff is 15.5 Å (Sun, 1998; Xiong et al., 2019). The Ewald method is used to describe the Coulomb forces, and the Atom based method is used for describing the van der Waals forces (Steinbach and Brooks, 1994).

The annealing simulation searches the potential energy surface by adding energy perturbations to obtain the lowest global energy configuration. The annealing simulation was performed in the Forcite module. Both the annealing cycles and the heating ramps per cycle are 10. The initial and maximum temperature were set as 300 and 600 K, respectively. The NVT (isochoric-isothermal ensemble) dynamics steps per ramp are 1000. The total simulation time is 200 ps, and the time step is 1 fs Andersen temperature control was used for the thermostat. The other settings are the same as the geometry optimization. The micropore volume and specific surface area of the 3-D kerogen structure model is calculated by CO_2 and N_2 molecular probe in the Atom volumes & surfaces tool of MS 2017.

It is well known that pores in both coal and kerogen have significant fractal characteristics. In this study, the Atom volumes & surfaces tool in MS 2017 enabled calculation of the pore volume in the 3-D kerogen structural model is calculated by varying the probe molecule size. Thus, the fractal dimension can be calculated as:

$$\frac{dV}{dv} \propto v^{1-D} \quad (2)$$

where V is total accessible volume of the 3-D kerogen structure model calculated by the probe molecule, v is the accessible volume of the probe molecule and D is the fractal dimension (Faulon et al., 1994; Pfeifer and Avnir, 1983).

4. Results

4.1. Geochemical information

The geochemical characteristics of the shale samples are given in Table 2. The OM types of the samples cover type I (Longmaxi shales), type II (Marcellus shale) and type III (Shanxi shales), TOC ranges from 0.75 wt% to 7.56 wt%.

4.2. Raman spectroscopy

The Raman spectra of the five kerogen samples are illustrated in Fig. 3. Two major peaks located between 1000–2000 cm^{-1} are D_1 and G bands, respectively. The D_1 band reflects lattice defects and vacancy

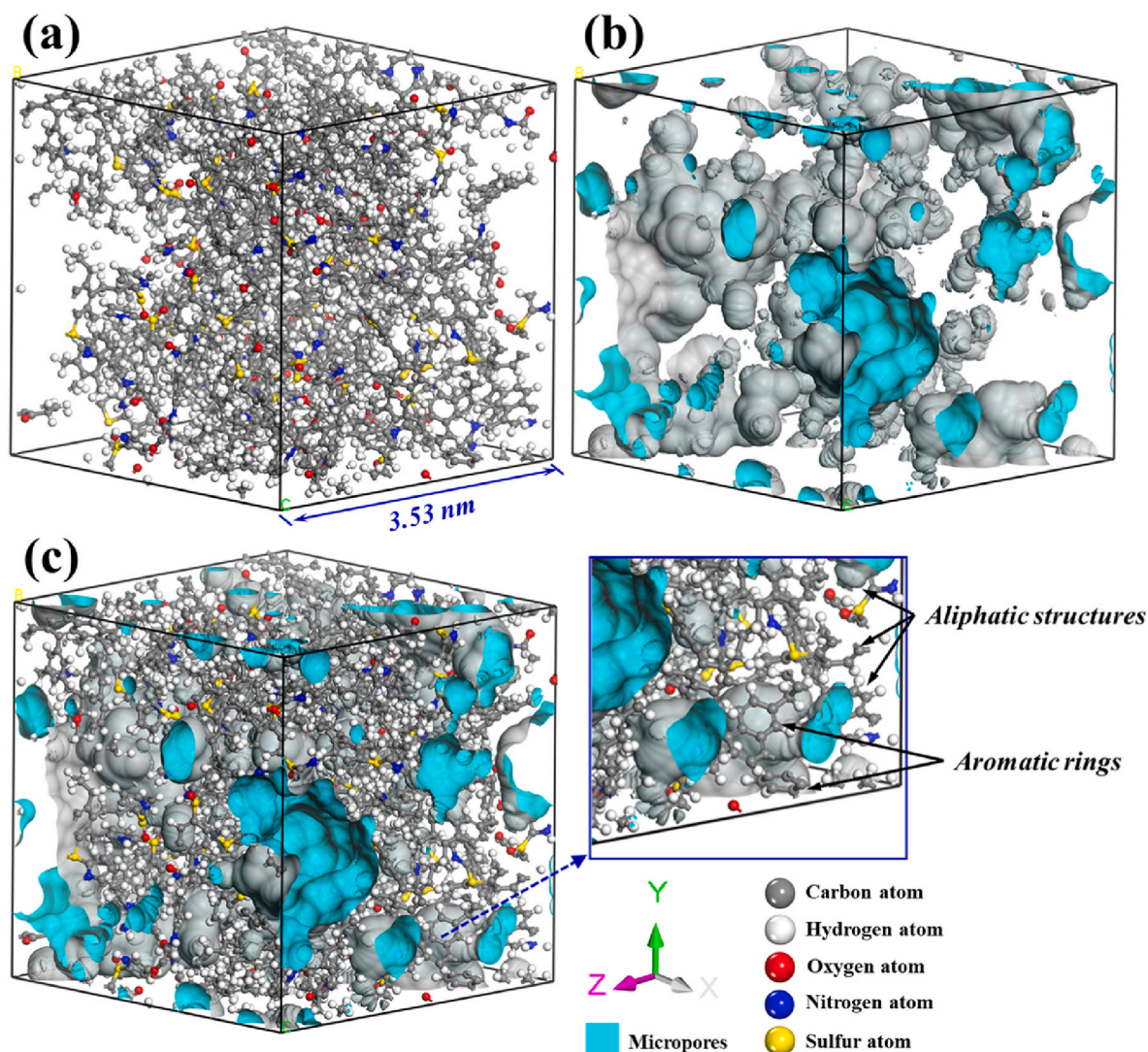


Fig. 10. 3-D structure of M-1 (a), micropores in M-1 (b), and the chemical structures that form micropores (c).

information between structural units, while the G band represents the graphite characteristic peak (Jehlička and Bény, 1992). Thus, the parameters of the D₁ and G bands can be used to evaluate the disorder degree of the kerogens. However, there is no agreement on the best parameter to evaluate disorder degree until now. The existing parameters include the area ratio (AD_1/AG), the intensity ratio (ID_1/IG) and FWHM (full widths at half mean for band) ratio of bands. Among these parameters, AD_1/AG and FWHM ratio are derived from the deconvolution methods, while ID_1/IG is obtained by automatic peak finding without any manual processing. Note that the parameters of disorder degree obtained by deconvolution methods are hard to be accepted by all researchers, because the results obtained from different deconvolution approaches are quite different (Henry et al., 2018). Thus, in this study, ID_1/IG is used to assess the disorder degree of kerogens. Raman parameters are shown in Table 3.

4.3. ¹³C NMR spectroscopy

The ¹³C NMR spectra can be divided into three regions as shown in Fig. 4: aliphatic (shift: 0–90 ppm), aromatic (shift: 100–156 ppm) and ketone/carbonyl carbons (shift: 160–230 ppm) (Trewheella et al., 1986). The peak intensity for the Marcellus (sample M-1) ($R_o = 1.13\%$) in the aliphatic part of the spectrum is significantly stronger than that of other samples. Meanwhile, the Marcellus (M-1) and Longmaxi (LMX-2 and

LMX-3) have similar thermal maturity but different peak intensity in the aliphatic part due to the different OM types. In contrast, peaks located in the aromatic part of the spectrum show higher intensities in all the samples with respect to peaks located in 160–230 ppm because oxygen-containing functional groups such as ketone and carbonyl carbons disappear before reaching the oil window (Tissot et al., 1974).

4.4. CO₂ and N₂ adsorption experiments

The CO₂ adsorption isotherms are shown in Fig. 5a. For all samples, the amount of adsorbed CO₂ shows a rapid increase at relatively low pressure followed by a slow increase at relatively high pressure. Note that the Marcellus (M-1) and Longmaxi (LMX-2 and LMX-3) have similar thermal maturity but different adsorption capacity due to differences in OM type. As shown in Fig. 5b, the pore size distribution curves exhibit a bimodal distribution with two distinct peaks: one large peak at 0.45–0.65 nm and a second small peak at 0.8–0.9 nm. The micropore volume is highest for type III samples (SX-1 and SX-2), and then for type II samples (M-1) and type I samples (LMX-2 and LMX-3).

According to the IUPAC classification, the N₂ adsorption/desorption curves of M-1 and SX-2 samples belong to Type IV isotherm (Fig. 6). Moreover, the shape of hysteresis loops indicates that the pore types of M-1 and SX-2 belong to H2 (inkbottle-shaped pore) and H3 (plate-like pore) respectively. Results from pore size distribution analysis suggest

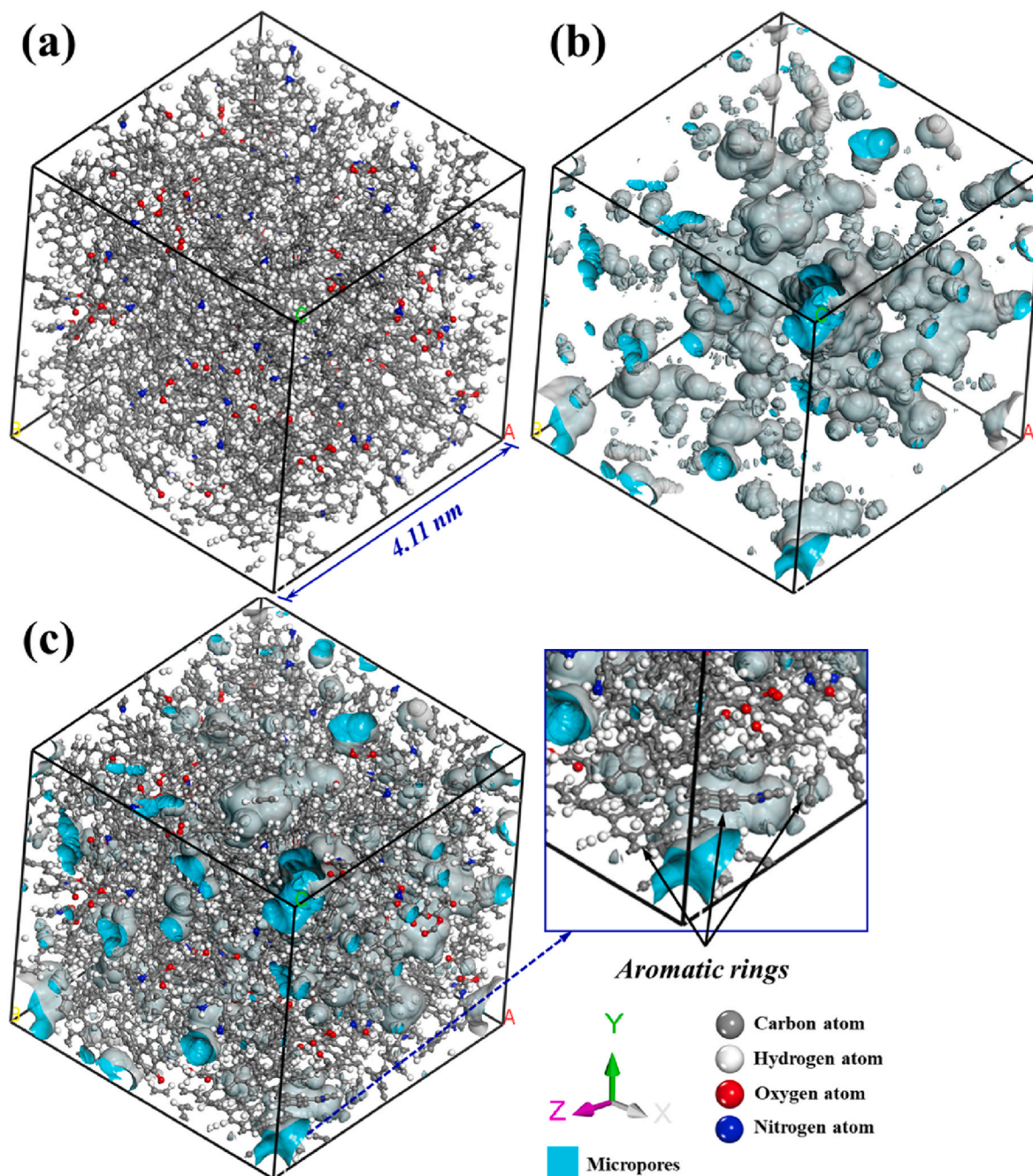


Fig. 11. 3-D structure of SX-2 (a), micropores in SX-2 (b), and the chemical structures that form micropores (c).

that sample M-1 has a higher pore volume of the pores of 2–140 nm.

5. Discussion

5.1. Differences in chemical compositions from ^{13}C NMR

The ^{13}C NMR parameters derived from deconvolution of the ^{13}C NMR spectra are shown in Table 4. It can be seen from the ^{13}C NMR parameters that aromatic structures are dominant in carbon skeleton of all kerogen samples ($f_a > 71.52\%$). For aromatic structures, the relative content of f_a^H and f_a^B is significantly greater than that of other aromatic structures. This means that aromatic carbons mainly exist in the form of protonated and bridgehead carbons. X_{BP} and X_b are usually used to characterize aromatic rings. As shown in Table 4, X_{BP} and X_b of SX-1 and SX-2 are 0.28 and 0.33, respectively. This suggests that kerogens of

Shanxi Formation have a high degree of condensation of aromatic rings. According to Faulon et al. (1994) and Wang et al. (2020), the larger X_{BP} in kerogens of Shanxi Formation show that 3×3 sized aromatic rings comprise a large fraction of the total of aromatic rings (Table 5). For aliphatic structures, the relative content of f_{al}^* and f_{al}^H is highest for M-1, and then for Longmaxi and Shanxi samples. Moreover, the relative content of f_a^S indicates that some alkyl chains still exist on the aromatic ring in M-1 kerogen.

5.2. Differences in 3-D kerogen models based on molecular simulation

Based on the workflow in Fig. 2, we constructed two 2-D models of kerogen structure using the Marcellus (M-1) and Shanxi (SX-2) shales as examples (Fig. 7). There are three reasons for choosing only these two samples in this study: 1) the construction of the kerogen models is time

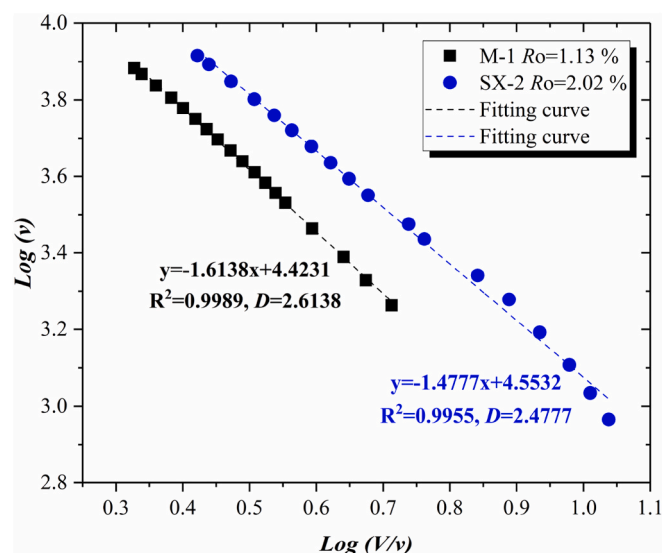


Fig. 12. Fractal characteristics of pores in 3-D kerogen structure.

consuming, 2) 3-D kerogen models of Marcellus and Shanxi Formation samples are absent in the literature, 3) in order to highlight the influences of chemical compositions on the development of micropore. Note that kerogen molecular model is an averaged result in this study because the chemical formula inferred from the ^{13}C NMR spectroscopy has multiple solutions. In this section, the accuracy of the models is verified by comparing the structural parameters of models with experimental measurements (Table 6), and then the differences between the two models are discussed in detail.

The relationships among the modeled atomic H/C and O/C ratios, Ro, and OM types are plotted on a Van Krevelen diagram (Fig. 7c). As shown in Fig. 7c, the results of H/C and O/C are in reasonable domains according to the predicated organic types and thermal maturities. The modeled H/C and O/C ratios of SX-2 (0.69 and 0.036) are close to Yan et al. (2015)'s experimental data (H/C: 0.56, O/C: 0.04) for the Shanxi Formation kerogen. For the M-1 sample, due to the absence of atomic ratio data for Marcellus (at the same maturity stage), we compared the modeled H/C and O/C ratios (1 and 0.057) with Weck et al., 2017's experimental data (H/C: 1.19, O/C: 0.08) of type II Kerogen. Moreover, the ^{13}C shifts from the simulated results agree well with those from experimental results (Fig. 8). Note that the quantity of S and N atoms cannot be evaluated because of the lack of quantitative experimental data - we will further improve this constraint in our future work.

For the chemical compositions in samples M-1 and SX-2, we found that the aliphatic carbons in M-1 are more abundant than in SX-2, while the aromatic carbons in SX-2 are more abundant than those in M-1 (Table 6). It was also found that some methyl groups and carbonyl functional groups were still present in SX-2 (Fig. 7), which is consistent with the observations of other researchers (Weck et al., 2017).

A series of 3-D models with different densities were generated by varying the periodic boundary conditions of 3-D model, enabling the relationship between total potential energy and density to be quantified after annealing simulation. As shown in Fig. 9, the total potential energy first decreases then increases with increasing density, and thus the location of the lowest total potential energy is the density of the kerogen structure model. Table 7 compared the thermodynamic properties of the kerogens that are modeled based on Ungerer et al. (2015)'s models and this study. Note that the differences in the thermodynamic properties between this study and the reported models (e.g., Ungerer et al., 2015) may be attributed to different sedimental conditions of the investigated samples. On the other hand, the densities of M-1 and SX-2 kerogens are 1.04 g/cm^3 and 1.16 g/cm^3 respectively, which is consistent with the densities reported by other researchers (type II kerogen: $1.0\text{--}1.15$

g/cm^3 , type III kerogen: $1.14 \pm 0.02 \text{ g/cm}^3$) (Mastalerz et al., 2012; Okiongbo et al., 2005; Ungerer et al., 2015). Note that the simulated density of kerogen is usually slightly lower than the actual density, because impurities (e.g., clay minerals and non-mineral trace elements) in kerogen tend to increase density.

3-D models of M-1 and SX-2 are shown in Figs. 10 and 11. It can be seen from Table 6 that the micropore volume and specific surface area of the two models calculated from CO_2/N_2 molecular probes are consistent with the results from gas adsorption experiments. By comparing the 3-D kerogen structures of M-1 and SX-2 (Figs. 10 and 11), we observe that the nature of the micropores is different. The micropores in M-1 are developed within volumes occupied by both aliphatic structures and aromatic structures, whereas the micropores in SX-2 are mainly developed within volumes dominated by aromatic rings. This means that the space of micropore development varies with the change of chemical compositions.

As shown in Fig. 12, the R^2 of the fitting curves of $\log(V/v)$ vs $\log(v)$ for M-1 and SX-2 are 0.9989 and 0.9955, respectively. This suggests that the pores in the 3-D kerogen structure exhibit fractal features. The fractal dimensions of M-1 and SX-2, calculated from Eq. (2) are 2.6138 and 2.4777, respectively. Based on fractal theory, the larger the fractal dimension, the more complex the pore morphology and the more fully the volume filled - larger fractal dimensions denote rougher, less-planar, surfaces. Thus, the pore morphology in sample M-1 (less mature, more aliphatic, Fig. 7) is more complex than that in SX-2 (more mature, more aromatic, Fig. 7). Hence, we can infer that the morphology of micropores developed in aliphatic structures is more complex than that developed in the aromatic structures.

5.3. Relationships between chemical structure and the development of micropores

5.3.1. Influences of chemical compositions on the development of micropores

The chemical structure of carbonaceous materials (coal/kerogen) has been widely studied (Yu et al., 2019). For coal, it has been found that micropores tend to develop in aliphatic chains and oxygen-containing functional groups (Liu et al., 2019). This begs the question as to whether the development of micropores in kerogen is intrinsically related to chemical structures?

Correlations between the micropore volume (from CO_2 adsorption experiment) and the relative content of chemical structures are shown in Fig. 13. It is evident from this diagram that the micropore pore volume increases with increasing f_a^A , X_{BP} , X_b and f_a^B (Fig. 13a, b, c, d), whereas it decreases with increasing f_a^H and f_a^S (Fig. 13e and f). This means that the reduction of aliphatic structures and the increase in aromatic structures are favorable for the development of micropores. These relationships in Fig. 13 further confirm the deduction that the development of micropore in kerogen is related to chemical composition.

5.3.2. Influences of disorder degree on the development of micropores

By comparing the relationships between the chemical compositions and disorder degree, it was found that I_{D1}/I_G is positively correlated with the parameters of aromatic rings but not correlated with other parameters (Fig. 14). This means that in mature kerogens, disorder degree is mainly reflected in the spatial arrangement of aromatic structures. In general, the spatial arrangement of structural groups varies with changes in chemical composition, because the overall kerogen structure tends to retain a stable low-energy state. This may indicate that the spatial arrangement associated with the change of chemical composition also influences micropore development. Considering that disorder degree is derived from the in-plane defects and vacancy between structural clusters, we infer that the disorder degree affects the development of micropores by changing the geometry and connectivity of voids between structural clusters. The strong positive correlation in Fig. 15 confirms the deduction that the development of micropore is also related to the

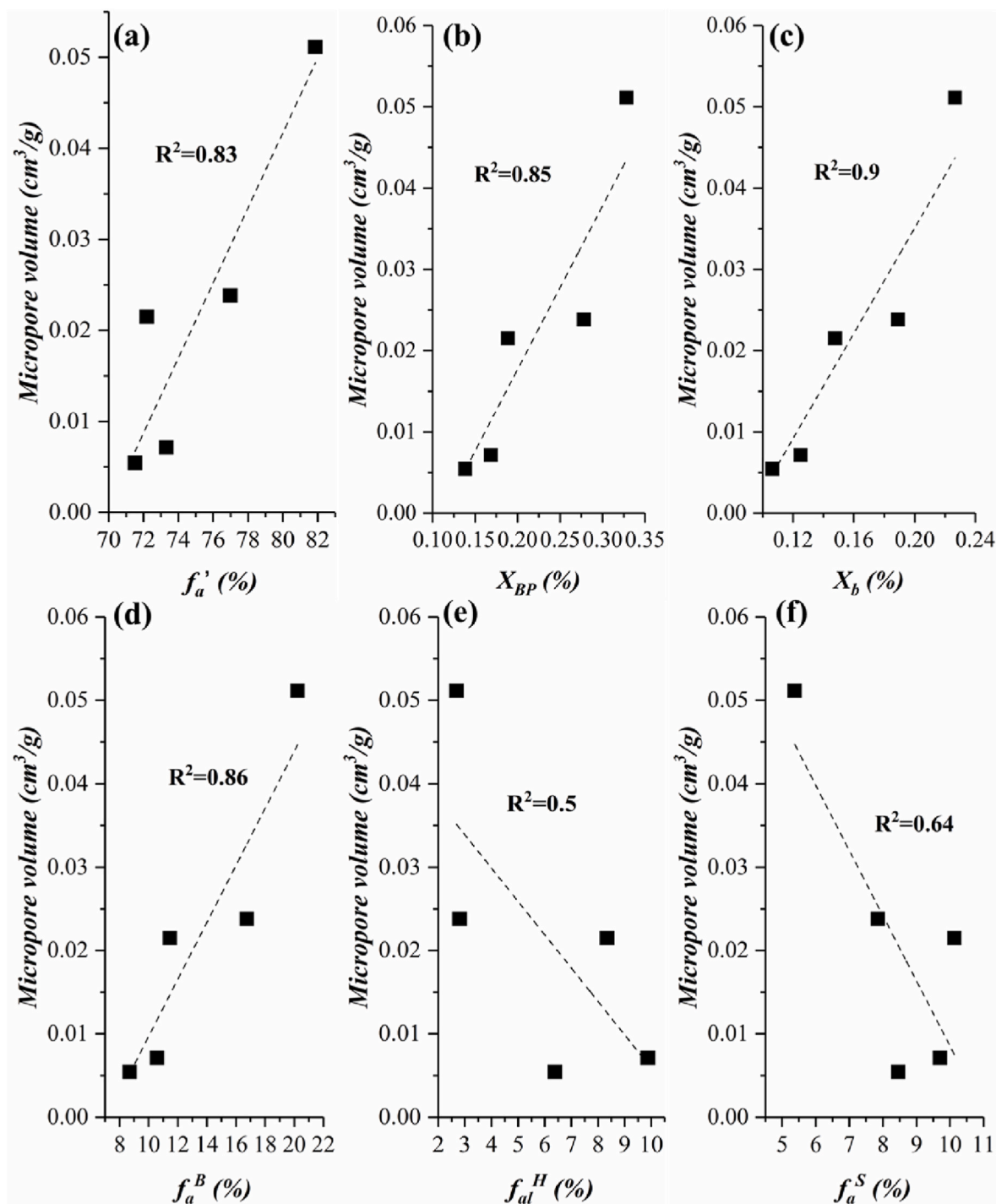


Fig. 13. Relationship between micropore volume and relative content of chemical structures.

spatial arrangement of chemical compositions.

5.3.3. Differences in the development of micropores in mature kerogen

By analyzing the influences of kerogen microstructure on the development of micropores, a suggested molecular-level mechanism of the differences in micropore development is illustrated in Fig. 16. For the M-1 kerogen, there are still some aliphatic structures that exist in kerogen, whereas the aromatic structures have not yet undergone polycondensation and stacking. The correlation between micropore volume and the relative content of chemical structures shows that the loss of aliphatic structures and the increase in aromatic structures are

favorable for the development of micropores. In addition, by comparing the fractal dimension and the chemical compositions of M-1 and SX-2, we found that the morphology of micropores developed in aliphatic structures is more complex than that developed in the aromatic structures. Therefore, both the 3-D models and ^{13}C NMR parameters indicate that the development of micropores is related to the chemical compositions.

For other kerogen samples, micropores are mainly developed within the spaces in aromatic structures. Moreover, the 3-D model of SX-2 shown in Section 5.2 found that the micropores are mainly developed in the inner aromatic layers. This means that in mature kerogens,

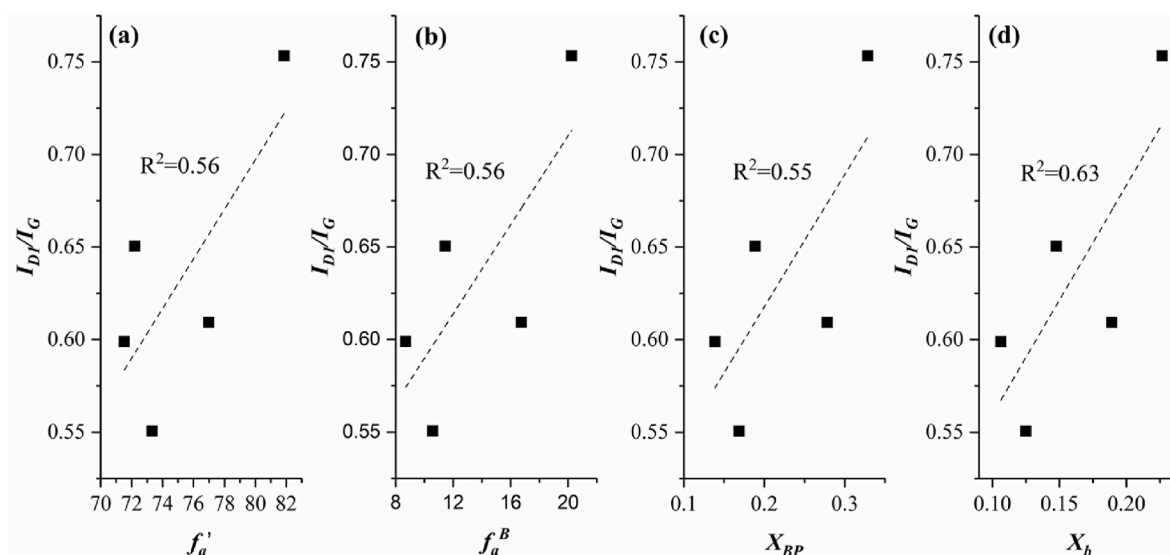


Fig. 14. Relationship of I_{D1}/I_G vs. ^{13}C NMR parameters.

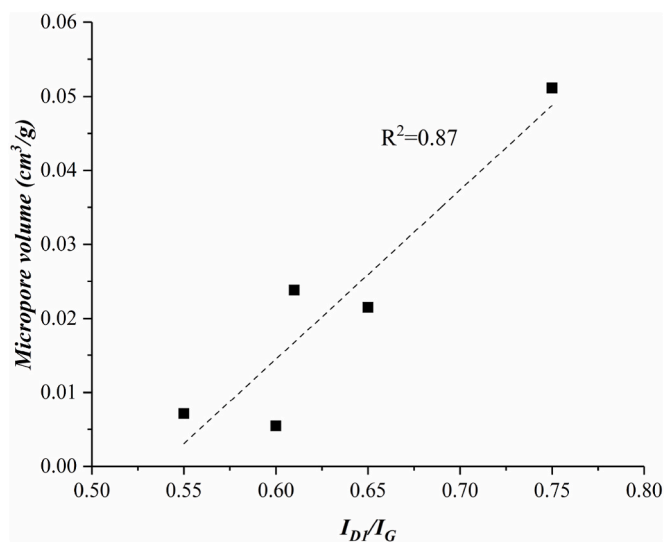


Fig. 15. Relationship between micropore volume and I_{D1}/I_G .

aromatic structures can significantly influence the development of micropores. The correlation between I_{D1}/I_G and micropore volume in Fig. 15 suggests that apart from chemical compositions, the development of micropores is also related to disordered structural clusters. On the other hand, the relationships between ^{13}C NMR parameters and I_{D1}/I_G indicate that in mature kerogens, disorder degree is mainly reflected by the spatial arrangement of aromatic structures. Thus, for mature kerogen, these disordered aromatic structures are favorable for the development of micropores. The mechanism is that with increasing disorder degree, void expansion between structural clusters results in the development of some micropores (Fig. 16). This may be one of the reasons why the micropore volume tends to decrease in over-mature stage, because graphitization will reduce the disorder degree of aromatic layers (Mastalerz et al., 2013). Moreover, using HRTEM, Romero-Sarmiento et al. (2014) and Wessely et al. (2020) also demonstrated this phenomenon by directly observing the micropores developed in disordered aromatic layer of kerogen. In short, the development of micropores is related to the surface properties of kerogen structure, including its chemical composition and spatial arrangement.

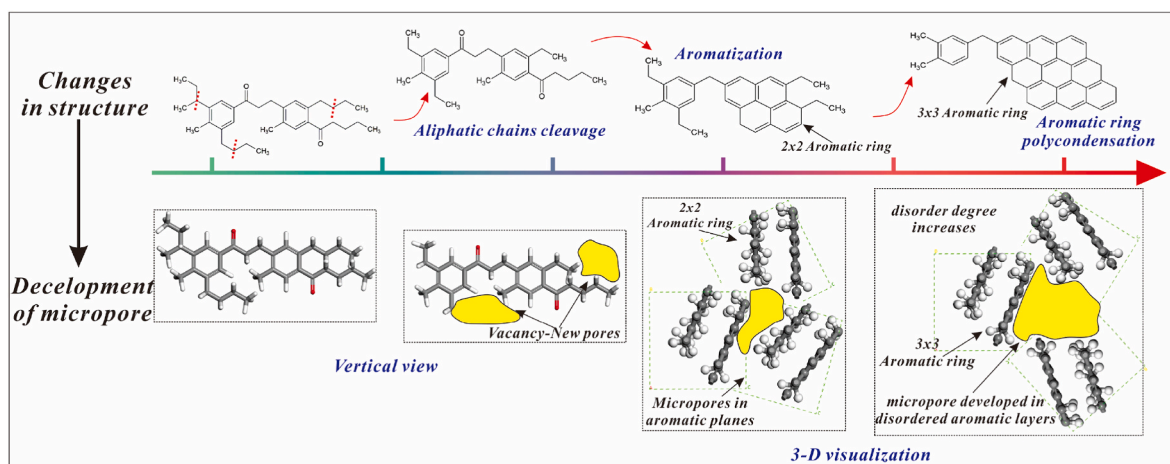


Fig. 16. Differences in the development of micropores.

6. Conclusion

- This study provides an improved methodology for the construction of a 3-D kerogen structure model, which reveals an integrated understanding of the organic geochemical and chemical structures together with thermodynamic and petrophysical properties of bulk kerogen. This method can be used to characterize the macromolecular structure in various kerogens.
- The correlation between micropore volume and the relative content of chemical structures shows that the loss of aliphatic structures and the increase in aromatic structures are favorable for the development of micropores. By comparing the 3-D kerogen structure of M-1 and SX-2, we found that the morphology of micropores developed in aliphatic structures is more complex than that developed in aromatic structures.
- The development of micropores is related to the surface properties of kerogen structure, including its chemical composition and spatial arrangement. For mature kerogens with a large proportion of aromatic rings, disordered aromatic structures are favorable for the development of micropores.

Credit author statement

Yanbin Yao: Conceptualization, Methodology, Supervision, Writing Reviewing and Editing, Project administration, and Funding acquisition. Chu Zhang: Validation, Writing Original draft preparation, Investigation. Derek Elsworth: Assist in collecting Marcellus shale, Writing Reviewing and Editing, Validation. Dexun Liu: Assist in collecting Shanxi Formation shale, Resources. Yiwen Ju Writing Reviewing and Editing. Yuguang Dong and Shun Ye: Investigation and Visualization.

Declaration of competing interest

The authors declare that they have no known competing financial interests or personal relationships that could have appeared to influence the work reported in this paper.

Acknowledgments

We acknowledge financial support from the National Natural Science Foundation of China (41872123; 41830427) and the National Major Science and Technology Projects of China (2017ZX05035).

References

Borrego, A., Prado, J., Fuente, E., Guillen, M., Blanco, C., 2000. Pyrolytic behaviour of Spanish oil shales and their kerogens. *J. Anal. Appl. Pyrolysis* 56, 1–21.

Bousige, C., Camelia Matei, G., Cathie, V.-G., Andrew E. P., Assiya, S., Gavin, V., Gaston, G., Mikhail, F., Christoph, W., Franz-Josef, U., Roland, J.-M.P., Benoit, C., 2016. Realistic molecular model of kerogen's nanostructure. *Nat. Mater.* 15, 576–582.

Faulon, J., Mathews, J., Carlson, G., Hatcher, P., 1994. Correlation between microporosity and fractal dimension of bituminous coal based on computer-generated models. *Energy Fuels* 8, 408–414.

Gregg, S.J., Sing, K.S.W., Salzberrg, H.W., 1967. Adsorption surface area and porosity. *J. Electrochem. Soc.* 114, 279C. <https://doi.org/10.1149/1.2426447>.

Henry, D.G., Jarvis, I., Gillmore, G., Stephenson, M., Emmings, J.F., 2018. Assessing low-maturity organic matter in shales using Raman spectroscopy: effects of sample preparation and operating procedure. *Int. J. Coal Geol.* 191, 135–151.

Hiroyuki, K., Ikuo, S., 2004. Interactions of organic liquids with coals: analysis by solid-state ^{13}C nuclear magnetic resonance. *Energy Fuels* 18, 1723–1731.

Huang, L., Ning, Z., Wang, Q., Qi, R., Cheng, Z., Wu, X., Zhang, W., Qin, H., 2019. Kerogen deformation upon CO_2/CH_4 competitive sorption: implications for CO_2 sequestration and enhanced CH_4 recovery. *J. Petrol. Sci. Eng.* 183, 106460. <https://doi.org/10.1016/j.petrol.2019.106460>.

Huang, L., Ning, Z., Wang, Q., Ye, H., Wang, Z., Sun, Z., Qin, H., 2018. Microstructure and adsorption properties of organic matter in Chinese Cambrian gas shale: experimental characterization, molecular modeling and molecular simulation. *Int. J. Coal Geol.* 198, 14–28.

Jehlička, J., Bény, C., 1992. Application of Raman microspectrometry in the study of structural changes in Precambrian kerogens during regional metamorphism. *Org. Geochem.* 18, 211–213.

Jacob, H., 1989. Classification, structure, genesis and practical importance of natural solid oil bitumen ("migrabitumen"). *Int. J. Coal Geol.* 11, 65–79.

Ju, Y., He, J., Chang, E., Zheng, L., 2019. Quantification of CH_4 adsorption capacity in kerogen-rich reservoir shales: an experimental investigation and molecular dynamic simulation. *Energy* 170, 411–422.

Landis, C.R., Castaño, J.R., 1995. Maturation and bulk chemical properties of a suite of solid hydrocarbons. *Org. Geochem.* 22, 137–149.

Lille, Ü., Heinmaa, I., Pehk, T., 2003. Molecular model of Estonian kukersite kerogen evaluated by ^{13}C MAS NMR spectra. *Fuel* 82, 799–804.

Liu, D., Xiao, X., Tian, H., Min, Y.S., Zhou, Q., Cheng, P., Shen, J.G., 2013. Sample maturation calculated using Raman spectroscopic parameters for solid organics: methodology and geological applications. *Chin. Sci. Bull.* 58, 1228–1241.

Liu, Y., Yao, Y., Liu, D., Zheng, S., Sun, G., Chang, Y., 2018. Shale pore size classification: an NMR fluid typing method. *Mar. Petrol. Geol.* 96, 591–601.

Liu, Y., Zhu, Y., Chen, S., 2019. Effects of chemical composition, disorder degree and crystallite structure of coal macromolecule on nanopores (0.4–150 nm) in different rank naturally-matured coals. *Fuel* 242, 553–561.

Loucks, R.G., Reed, R.M., Ruppel, S.C., Jarvie, D.M., 2009. Morphology, genesis, and distribution of nanometer-scale pores in siliceous mudstones of the Mississippian Barnett Shale. *J. Sediment. Res.* 79, 848–861.

Mastalerz, M., Schimmelmann, A., Drobnik, A., Chen, Y., 2013. Porosity of Devonian and Mississippian New Albany Shale across a maturation gradient: insights from organic petrology, gas adsorption, and mercury intrusion. *Am. Assoc. Petrol. Geol. Bull.* 97, 1621–1643.

Mastalerz, M., Schimmelmann, A., Lis, G.P., Drobnik, A., Stankiewicz, A., 2012. Influence of maceral composition on geochemical characteristics of immature shale kerogen: insight from density fraction analysis. *Int. J. Coal Geol.* 103, 60–69.

Mosher, K., He, J., Liu, Y., Rupp, E., Wilcox, J., 2013. Molecular simulation of methane adsorption in micro- and mesoporous carbons with applications to coal and gas shale systems. *Int. J. Coal Geol.* 109, 36–44.

Nguyen, C., Do, D.D., 2001. The Dubinin–Radushkevich equation and the underlying microscopic adsorption description. *Carbon N. Y.* 39, 1327–1336.

Okiongbo, K., Aplin, A., Larter, S., 2005. Changes in type II kerogen density as a function of maturity: evidence from the Kimmeridge Clay Formation. *Energy Fuels* 19, 2495–2499.

Patience, R., Mann, A., Poplett, L.J.F., 1992. Determination of molecular structure of kerogens using ^{13}C NMR spectroscopy: II. The effects of thermal maturation on kerogens from marine sediments. *Geochem. Cosmochim. Acta* 56, 2725–2742.

Pfeifer, P., Avnir, D., 1983. Chemistry in noninteger dimensions between two and three. I. Fractal theory of heterogeneous surfaces. *J. Chem. Phys.* 79, 3558–3565.

Rexer, T.F., Mathia, E.J., Aplin, A.C., Thomas, K.M., 2014. High-pressure methane adsorption and characterization of pores in Posidonia shales and isolated kerogens. *Energy Fuels* 28, 2886–2901.

Romero-Sarmiento, M.-F., Rouzaud, J.-N., Bernard, S., Deldicque, D., Thomas, M., Littke, R., 2014. Evolution of Barnett Shale organic carbon structure and nanostructure with increasing maturation. *Org. Geochem.* 71, 7–16.

Steinbach, P.J., Brooks, B.R., 1994. New spherical-cutoff methods for long-range forces in macromolecular simulation. *J. Comput. Chem.* 15, 667–683.

Sun, H., 1998. COMPASS: an ab initio force-field optimized for condensed-phase applications-overview with details on alkane and benzene compounds. *J. Phys. Chem. B* 102, 7338–7364.

Tissot, B.P., Durand, B., Espitalié, J., Combaz, A., 1974. Influence of nature and diagenesis of organic matter in formation of petroleum. *Am. Assoc. Petrol. Geol. Bull.* 58, 499–506.

Tong, J., Han, X., Wang, S., Jiang, X., 2011. Evaluation of structural characteristics of Huadian oil shale kerogen using direct techniques (Solid-State ^{13}C NMR, XPS, FT-IR, and XRD). *Energy Fuels* 25, 4006–4013.

Trewhella, M.J., Poplett, L.J.F., Grint, A., 1986. Structure of Green River oil shale kerogen: determination using solid state ^{13}C n.m.r. spectroscopy. *Fuel* 65, 541–546.

Ungerer, P., Collet, J., Yiannourakou, M., 2015. Molecular modeling of the volumetric and thermodynamic properties of kerogen: influence of organic type and maturity. *Energy Fuels* 29, 91–105.

Wang, X., Zhu, Y., Liu, Y., Li, W., 2019. Molecular structure of kerogen in the Longmaxi shale: insights from solid state NMR, FT-IR, XRD and HRTEM. *Acta Geol. Sin. Ed.* 93, 1015–1024.

Wang, X., Zhu, Y., Song, Y., Mathews, J.P., 2020. Structure and partial ordering of terrestrial kerogen: insight from high-resolution transmission electron microscopy. *Fuel* 281, 118759.

Weck, P.F., Kim, E., Wang, Y., Kruichak, J.N., Mills, M.M., Matteo, E.N., Pellenq, R.J.-M., 2017. Model representations of kerogen structures: an insight from density functional theory calculations and spectroscopic measurements. *Sci. Rep.* 7, 7068.

Wessely, V., Misch, D., Issa, I., Kiener, D., Fink, R., Seemann, T., Liu, B., Rantitsch, G., Sachsenhofer, R.F., 2020. Nanoscale pore structure of Carboniferous coals from the Ukrainian Donets Basin: a combined HRTEM and gas sorption study. *Int. J. Coal Geol.* 224, 103484.

Xiong, J., Liu, X., Liang, L., Wei, X., Xu, P., 2019. Investigation of the factors influencing methane adsorption on illite. *Energy Sci. Eng.* 7, 3317–3331.

Xiong, J., Liu, X., Liang, L., Zeng, Q., 2017. Adsorption of methane in organic-rich shale nanopores: an experimental and molecular simulation study. *Fuel* 200, 299–315.

Yan, D., Huang, W., Zhang, J., 2015. Characteristics of marine-continental transitional organic-rich shale in the Ordos Basin and its shale gas significance. *Earth Sci. Front.* 22, 197–206.

Yao, Y., Liu, J., Liu, D., Chen, J., Pan, Z., 2019. A new application of NMR in characterization of multiphase methane and adsorption capacity of shale. *Int. J. Coal Geol.* 201, 76–85. <https://doi.org/10.1016/j.coal.2018.11.018>.

Yu, K., Shao, C., Ju, Y., Qu, Z., 2019. The genesis and controlling factors of micropore volume in transitional coal-bearing shale reservoirs under different sedimentary environments. *Mar. Petrol. Geol.* 102, 426–438. <https://doi.org/10.1016/j.marpetgeo.2019.01.003>.

Zhang, C., Chen, Shangbin, Liu, Y., Chen, Si, Li, X., 2019. Mechanism of methane adsorption on groove space in organic matter surface. *Mol. Simulat.* 45, 186–198.

Zhao, T., Li, X., Ning, Z., Zhao, H., Li, M., 2018. Molecular simulation of methane adsorption on type II kerogen with the impact of water content. *J. Petrol. Sci. Eng.* 161, 302–310. <https://doi.org/10.1016/j.petrol.2017.11.072>.